Hydrographic Preconditioning for Seasonal Sea Ice Anomalies in the Labrador Sea

Citation: Fenty, Ian, and Patrick Heimbach. "Hydrographic Preconditioning for Seasonal Sea Ice Anomalies in the Labrador Sea." Journal of Physical Oceanography 43, no. 5 (May 2013): 863-883. © 2013 American Meteorological Society

As Published: http://dx.doi.org/10.1175/JPO-D-12-064.1

Publisher: American Meteorological Society

Persistent URL: http://hdl.handle.net/1721.1/82887

Version: Final published version: final published article, as it appeared in a journal, conference proceedings, or other formally published context

Hydrographic Preconditioning for Seasonal Sea Ice Anomalies in the Labrador Sea

IAN FENTY

Jet Propulsion Laboratory, Pasadena, California

PATRICK HEIMBACH

Massachusetts Institute of Technology, Cambridge, Massachusetts

(Manuscript received 29 March 2012, in final form 25 October 2012)

ABSTRACT

This study investigates the hydrographic processes involved in setting the maximum wintertime sea ice (SI) extent in the Labrador Sea and Baffin Bay. The analysis is based on an ocean and sea ice state estimate covering the summer-to-summer 1996/97 annual cycle. The estimate is a synthesis of in situ and satellite hydrographic and ice data with a regional coupled $1/3°$ ocean–sea ice model. SI advective processes are first demonstrated to be required to reproduce the observed ice extent. With advection, the marginal ice zone (MIZ) location stabilizes where ice melt balances ice mass convergence, a quasi-equilibrium condition achieved via the convergence of warm subtropical-origin subsurface waters into the mixed layer seaward of the MIZ.

An analysis of ocean surface buoyancy fluxes reveals a critical role of low-salinity upper ocean (100 m) anomalies for the advancement of SI seaward of the Arctic Water–Irminger Water Thermohaline Front. Anomalous low-salinity waters slow the rate of buoyancy loss–driven mixed layer deepening, shielding an advancing SI pack from the warm subsurface waters, and are conducive to a positive surface meltwater stabilization enhancement (MESEM) feedback driven by SI meltwater release. The low-salinity upper-ocean hydrographic conditions in which the MESEM efficiently operates are termed sea ice–preconditioned waters (SIPW).

The SI extent seaward of the Thermohaline Front is shown to closely correspond to the distribution of SIPW. The analysis of two additional state estimates (1992/93, 2003/04) suggests that interannual hydrographic variability provides a first-order explanation for SI maximum extent anomalies in the region.

1. Introduction

Sea ice variability in the Labrador Sea and Baffin Bay (LS&BB) is of climatic interest because of its relationship to deep convection and mode water formation (Visbeck et al. 1995; Pickart et al. 2002), its role in modulating carbon uptake and sequestration (DeGrandpre et al. 2006), and its influence on Northern Hemisphere atmospheric circulation patterns (Deser et al. 2004). The maximum wintertime extent of seasonal sea ice in the Labrador Sea, monitored via satellite passive microwave radiometry since the late 1970s, has generally declined since the early 1990s (Fig. 1). This trend has occurred in conjunction with significant decadal-scale atmospheric and hydrographic variability in the North Atlantic, such as the weakening of the subpolar gyre (Häkkinen and Rhines 2004), shifting surface circulation patterns (Häkkinen and Rhines 2009), a decline and rebound of the Labrador Current (Han et al. 2010), a redistribution of North Atlantic water masses including a warming and salinification of the interior Labrador Sea (Yashayaev 2007), and a reduction in typical convective mixing depths (Lavender et al. 2002; Våge et al. 2009).

Over this same period, the number and quality of in situ hydrographic observations in the Labrador Sea has dramatically increased owing to field campaigns (e.g., the Labrador Sea Experiment) and the expansion of the Argo network (Lavender et al. 2000, 2002; Straneo et al. 2003). Nevertheless, limited progress has been made toward understanding the relationship between hydrographic variability and sea ice extent. Arguably the biggest impediment has been in interpreting these new data to draw credible inferences about the details of the

Corresponding author address: Ian Fenty, Jet Propulsion Laboratory, California Institute of Technology M/S 300-323, 4800 Oak Grove Dr., Pasadena, CA 91109-8099.
E-mail: ian.fenty@jpl.nasa.gov

DOI: 10.1175/JPO-D-12-064.1

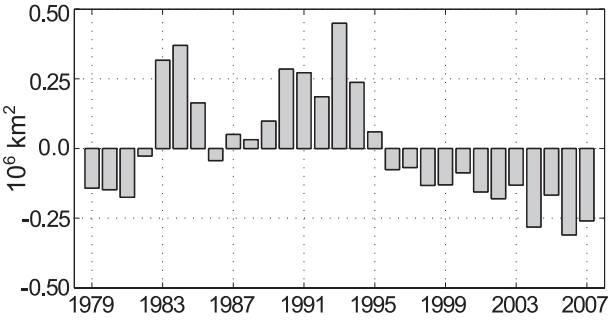

FIG. 1. Total sea ice area anomaly for March in the LS&BB (1979–2007), based on satellite data distributed by the National Snow and Ice Data Center (Comiso and Nishio 2008). Mean is 1.4×10^6 km^2.

temporal and spatial coevolution of the sea ice–ocean system. The construction of a coupled sea ice–ocean state estimate of the LS&BB by Fenty and Heimbach (2013, hereafter referred to as FH13) is a step toward overcoming this impediment. The estimate consists of a synthesis of a regional 30 km ($\approx 1/3°$) coupled sea ice–ocean model (Losch et al. 2010; Heimbach et al. 2010) with a suite of contemporary in situ and satellite hydrographic and sea ice (SI) observations by means of the Lagrange multiplier method (Wunsch and Heimbach 2007). FH13 introduced the state estimate and demonstrated its utility in an initial, data-constrained budget analysis.

Here, the analysis is extended through investigating the physical processes responsible for maximum ice extent variability with a focus on the evolution of sea ice into its maximum annual extent and marginal ice zone (MIZ) processes. Of primary interest is understanding the role which local air–sea fluxes and oceanic vertical mixing play in setting the MIZ relative to lateral advection of sea ice and oceanic heat and freshwater fluxes. Of the two main classes of hypotheses regarding dominant controls on maximum ice extent variability in the LS&BB, none has been found satisfactory at explaining the observed variability.

a. Atmosphere-centric hypotheses

Most hypotheses explaining interannual ice variability in the Labrador Sea invoke atmospheric variability on seasonal (or longer) time scales. Rogers and Van Loon (1979) showed that ice anomalies were positive (negative) during years associated with an anomalously deep (shallow) Icelandic Low and a shallow (deep) Azores High, a sea level pressure pattern that is correlated with cold dry continental air advection over the LS&BB. Today, the sea level pressure pattern identified by Rogers and Van Loon (1979) is described as the North Atlantic Oscillation (NAO), the leading eigenvector of the North Atlantic sea level pressure, with variability described by its associated scalar eigenvalue index (Hurrell 2008).

Later model and observational studies have explored the connection between sea ice anomalies and large-scale atmospheric variability in the North Atlantic (e.g., Mysak et al. 1996; Prinsenberg et al. 1997; Krahmann and Visbeck 2003; Deser and Teng 2008). However, open questions remain about the salient mechanisms and processes involved. For example, what is the relative importance of dynamical processes (e.g., sea ice advection from wind anomalies) versus thermodynamic processes (e.g., sea ice production from air–sea heat flux anomalies) in establishing the maximum wintertime sea ice extent?

Atmosphere-centric hypothesis are attractive because increases of sea ice production and wind-driven advection during anomalously cold, dry, and windy winters are physically plausible. Complicating the picture, however, is that the maximum temporal correlation between NAO and Labrador Sea sea ice extent anomalies occurs at a 1-yr lag (Stern and Heide-Jøargensen 2003). As virtually all ice in the LS&BB is seasonal, the lagged correlation suggests a role for interannual hydrographic variability. It also bears noting that coupled sea ice–ocean models forced with observed atmospheric fields do not reliably reproduce the observed interannual sea ice extent variability (e.g., Ikeda et al. 1988).

b. Ocean-centric hypotheses

The amount of enthalpy which must be removed from a column of seawater to produce ice is a function of the vertical distribution of heat and salt. The resulting seawater temperature change, and hence sea ice production propensity, for a given loss of enthalpy is greater in a column with a shallow and highly stratified surface layer. With a sufficiently high initial stratification, surface waters can maintain their isolation from warmer subsurface waters despite negative surface buoyancy fluxes from surface heat loss, or the release of high-salinity brine released during ice growth.

Observational support for ocean-centric hypotheses comes from positive sea ice anomalies that reappeared each winter in concurrence with the propagation of a low-salinity anomaly around the subpolar gyre during the Great Salinity Anomaly of the 1960s (Mysak and Manak 1989). An important caveat of the study was that the data could not reveal whether salinity anomalies induced ice anomalies, or vice versa. Marsden et al. (1991) and Deser et al. (2002) provide further evidence of lagged negative correlation between the anomalies of upper-ocean salinity and sea ice extent anomalies. Despite these data, the mechanisms connecting salinity and sea ice extent anomalies on the basin scale remain unknown.

In section 2, we formulate a novel hypothesis that will be investigated in the remainder of this paper. To aid the discussion the reader should refer to Fig. 2 in FH13 for a schematic of the domain's upper-ocean circulation and identification of locations referred to in the following text. Our first analysis elucidates the role of sea ice and ocean tracer advection in the expansion of ice across the domain. To do so, in section 3 we compare the evolution of ice extent in the state estimate with one obtained using a simple one-dimensional coupled thermodynamic sea ice–ocean mixed-layer model. A detailed investigation of water mass properties and sea ice–ocean feedbacks in the marginal ice zone and across the Thermohaline Front is presented in section 4. We provide evidence for what we term the *meltwater stabilization enhancement mechanism* (MESEM) and its relation to *sea ice–preconditioned waters* (SIPW). Section 5 concludes with a discussion of our main findings. For reference, the common acronyms are defined in Table 1.

2. A new hypothesis for maximum ice extent variability

A connection between the maximum ice extent and atmospheric–hydrographic variability can be deduced by examining the ranges of observed ice extents, the maximum ice-covered area less the minimum, through time (FH13, Fig. 1). During autumn and winter, the lateral expansion of sea ice ceases upon encountering either a coast or unfavorable atmospheric or oceanic conditions. When ice expansion is limited by coastal geometry, such as the in the central Arctic, the ranges of observed wintertime ice extent are small relative to their medians. In the LS&BB, the range of wintertime ice extent scales as roughly half of the median with the greatest range in March—the month with the maximum mean ice cover. Therefore, the atmosphere and ocean must be the primary source of variability in the LS&BB.

The patterns of ice maximum extent variability can be derived from satellite observations, 1979–present (Comiso and Nishio 2008), and presatellite era reconstructions, 1953–77 (Walsh and Johnson 1979). These patterns indicate that each year the ice reaches as far south as the climatological position of the Thermohaline Front (THF) separating the cold fresh Arctic Water (AW) (wintertime $\theta \approx -1.8$°C, $S \leq 34.5$) of Baffin Bay with the warmer and saltier subtropical-origin Irminger Waters (IW) ($\theta \approx 4.3$°C, $S \approx 34.9$) found in the northern Labrador Sea and southeastern Baffin Bay. A diagram of the climatological THF in the domain can be found in Fig. 3 of FH13. All observed wintertime sea ice maximum extent variability, therefore, occurs seaward of the THF (Fig. 2a). Specifically, the highest mean March ice concentration variance in the Labrador Sea north of 55°N is almost exclusively between the THF and the 3000-m isobath (Fig. 2b).

Observations made during two field campaigns, which aimed to elucidate sea ice–atmosphere–ocean processes in the MIZ, the summer 1984 Marginal Ice Zone Experiment (MIZEX-84) (Morison et al. 1987), and the spring 1990 Labrador Ice Margin Experiment (LIMEX) (Carsey et al. 1989), hint that the operation of a sea ice–boundary layer stabilization feedback may be a critical missing component to understanding sea ice maximum extent variability.

During MIZEX-84, an instrumented ice floe was driven by winds from a position 60 km behind the ice edge toward the MIZ and eventually into open water in the Greenland Sea. As the MIZEX floe approached the MIZ, ice ahead was progressively driven across the MIZ and subsequently melted in the warmer Atlantic Water. During its transit, the floe encountered cold fresh surface waters in a very shallow (~20 m) mixed layer—the remnants of melted ice that had preceded it. Measured ice basal ablation rates in the cold shallow mixed layer were very low. At the location of the former ice edge, the floe encountered a warmer, deeper, and saltier mixed layer. Basal melt rates subsequently increased from 2 to 5 cm day^{-1}, which increased the release of buoyant ice meltwater into the mixed layer. With the addition of meltwater, the mixed layer freshened, stabilized, and shoaled from 25 m to ≤5 m, the ice–buoyancy feedback described by McPhee (1983). Sensible heat losses from turbulent ocean–ice and air–sea heat fluxes in the shallow stratified layer caused seawater temperatures to fall, which then reduced basal melt rates to the levels observed in the cold waters behind the MIZ.

Ocean measurements taken in waters seaward of the Labrador shelfbreak during LIMEX found a cold, fresh, highly stratified, and shallow (~20 m) mixed layer (Tang 1992). Because the depth of the mixed layer encountered was much shallower than the typical mixed layer depths of the AW found on the Labrador Shelf, cross-shelf AW transport was ruled out as the source of the low salinity waters. Instead, the freshwater anomaly was thought to be due to an earlier unobserved episode of ice melt, possibly from ice advected off the shelf by a boundary current eddy or an episode of strong offshore winds.

Both campaigns suggest the importance of a sea ice–ocean feedback wherein dynamical convergence of ice into waters and initially unfavorable to in situ ice growth (e.g., weakly stratified) and/or its extended persistence (e.g., high enthalpy) eventually changes the hydrographic conditions so as to make them conducive to ice growth and/or extended persistence. Indeed, the melting of the MIZEX-84 floe in the warm waters beyond the

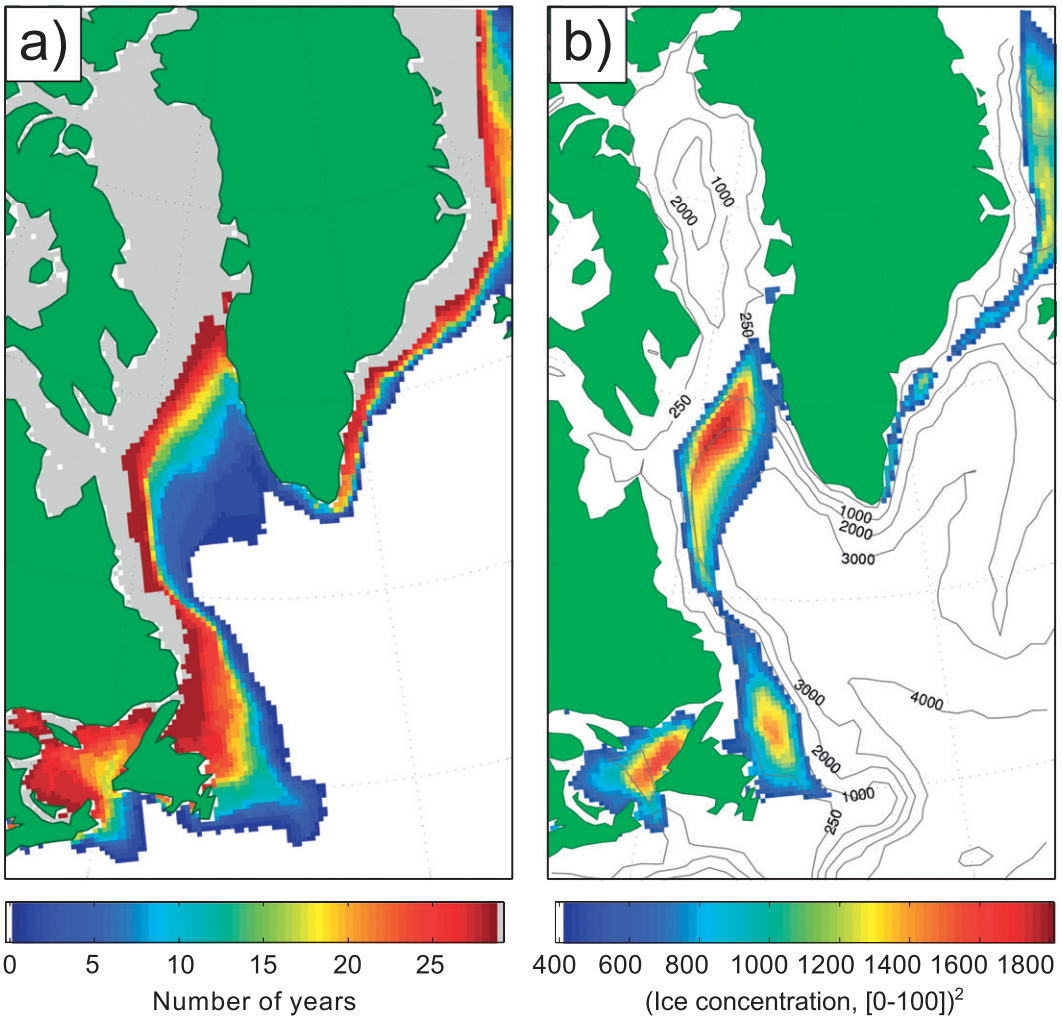

FIG. 2. Histogram of (a) monthly mean sea ice extent and (b) mean March sea ice concentration variance derived from satellite SSM/I ice concentration (1979–2008).

MIZ may have caused the reduction of its observed basal melt rates by 1) shoaling the mixed layer following the addition of fresh buoyant ice meltwater and 2) reducing the temperature of the shoaled mixed layer following ocean–ice sensible heat fluxes. One would expect that floes advected off the Labrador Shelf would persist longer when encountering cold, fresh highly stratified waters such as those observed during LIMEX than the warm, salty weakly stratified waters more commonly found there. Indeed, Tang (1992, p. 170) speculated that as the ice drifts across the shelfbreak and melts, it " . . . gradually modifies the temperature and salinity of the upper water column until an equilibrium state is reached in which the eastward ice velocity is equal to the rate of ice-edge melt."

While neither campaign directly observed the modification of upper-ocean hydrography from sea ice–ocean interaction during the expansion of sea ice to its maximum extent, we hypothesize that a sea ice–ocean feedback may be important for significant ice edge advancement beyond the THF in the Labrador Sea.

We term the progressive boundary layer stabilization in the marginal ice zone by buoyant sea ice meltwater release that permits the lateral expansion of ice into waters initially unfavorable for in situ thermodynamic production the MESEM. The central theme of this paper is to investigate the role the MESEM plays in establishing and maintaining the sea quasi-equilibrium state, the approximate steady state achieved in midwinter with respect to ice edge location, ice thicknesses, and ice concentration.

3. One-dimensional thermodynamic analyses

One-dimensional (1D) thermodynamic mixed layer analyses are conducted to determine where sea ice cover

is predictable in the absence of lateral oceanic and sea ice transport.

There are three notable differences between the approach taken here and earlier studies (e.g., Ikeda et al. 1988): 1) the predictability calculations are made with an ocean state that is initialized before the appearance of significant ice in the Baffin Bay—earlier studies initialized their models after Baffin Bay freeze-up; 2) the initial ocean state is taken from a state estimate—earlier studies initialized the ocean state from climatologies; and 3) the air–sea heat fluxes used to drive the model are taken from the state estimate—earlier studies used ad hoc methods to generate atmospheric fields from meteorological data collected from sparse coastal and ocean platform weather stations.

a. Experimental method

The 1D ocean mixed layer model parameterizes convective mixing triggered by surface buoyancy loss–driven static instability. The region is decomposed into 4284 noninteracting 1D columns that are each initialized with a T and S profile from the 1996/97 state estimate of FH13. Each column is independently forced with daily averaged air–sea heat fluxes from the state estimate.

Mixed layer static stability is determined at the end of each time step by comparing the potential density in the mixed layer with that of the next deepest cell. In the event of instability, the mixed layer deepens into the next deepest cell, entraining its enthalpy and salt. Sea ice is considered present when the mixed layer attains a temperature of -1.96°C and is stable to small positive salinity perturbations (representing salt release triggered by 2 cm of ice growth). Mixing of the upper ocean by mechanical processes (shear instabilities) is parameterized by first homogenizing T and S in the upper 45 m. Experiments were initialized from different ocean conditions corresponding to dates between August and December. With minor exceptions, the results are independent of initialization date. Therefore, only the 1 October initialization is described.

b. Analysis

The dates of predicted sea ice formation are compared with the observed ice edge for three periods (Fig. 3). The models accurately predict the ice formation date over much of the domain during the simulation. In particular, the observed 1 December ice edge is predicted in Baffin Bay, across Davis Strait, and in the northwestern Labrador Sea around Baffin Island—regions with similar distributions of surface AW. The later expansion of ice across eastern Davis Strait and south along the Labrador Current and Newfoundland is also captured.

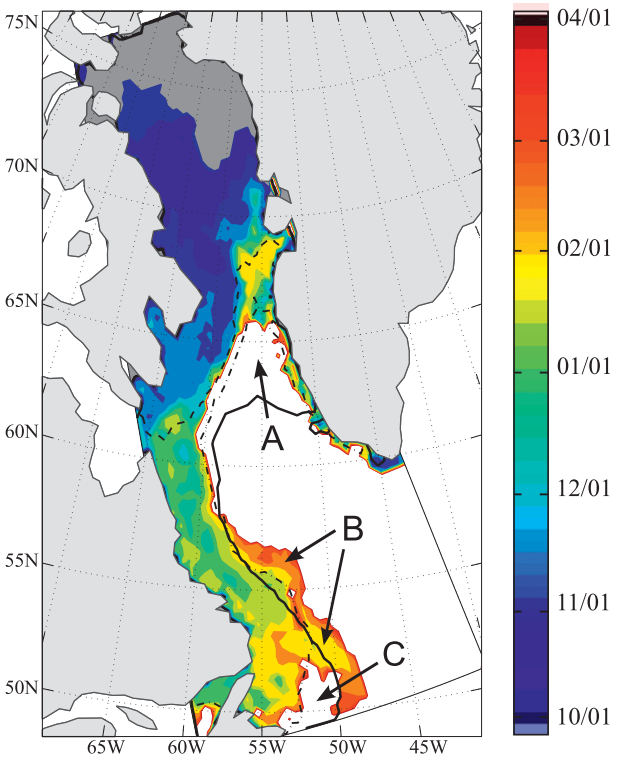

FIG. 3. Dates of sea ice formation in the 1996/97 annual cycle as predicted by the 1D models (colors) and the observed locations of the sea ice edge (lines). Dark gray denotes existing ice on 1 October. White denotes no ice formed during the simulations. Observed ice edge locations: 1 Dec (dashed line), 1 Feb (dash-dotted line), and 10 Mar (solid line). Letters (A, B, and C) denote areas of significant discrepancies between the 1D models and observations.

After 1 February, the mixed layer models fail to reproduce the observed ice expansion. Three areas are most notable for their discrepancy. The first region is the Northern Slope, the northern part of the LS above the 3000-m isobath [Northern slope (NS)], of the Labrador Sea (A). The 1D models cannot reproduce the observed expansion of ice on the IW-side of the THF. Two factors are likely to explain this discrepancy: missing ice advection and an inconsistent upper-ocean stratification. A nonzero component of ice velocity normal to the ice edge is found in the state estimate (FH13), suggesting the importance of cross-THF sea ice advection. An inconsistent upper-ocean stratification in (A) is possible because of the missing lateral transport of AW from the inner shelf component of the West Greenland Current (WGC).

In discrepancy area (B), ice is predicted seaward of the Labrador slope south of 57°N where no ice is observed. The hydrographic situation in the state estimate on 1 October includes a tongue of residual ice meltwater propagating southward out of the domain in exactly the same location. In the state estimate, the meltwater tongue

TABLE 1. Abbreviations used frequently in this paper.

AW	Arctic Water
IW	Irminger Water
LS&BB	Labrador Sea & Baffin Bay
MESEM	Meltwater stability enhancement mechanism
MIZ	Marginal Ice Zone
NEC	Northeast corner
NS	Northern slope
SIPW	Sea ice–preconditioned water
THF	Thermohaline Front
WGC	West Greenland Current

disperses by 1 February. Therefore, excessive ice at (B) is most likely an artifact of missing lateral ocean transport.

At (C), the 1D models fail to predict the appearance of ice on Newfoundland Shelf south of 53°N. Yao and Ikeda (1990) found that the transport of sea ice and cooled waters from the northern Labrador Shelf was required for ice to extend around Newfoundland and the Grand Banks, a conclusion confirmed by our experiment.

The 1D model simulations reveal where ocean and sea ice advection is required for the accurate prediction of the ice edge: on the IW side of the THF in the NS and along the southernmost part of the Labrador Shelf. A separate experiment in which the atmospheric state is perturbed would potentially reveal the atmospheric control on ice development in the absence of lateral transports but is beyond the scope of this study.

4. Sea ice quasi-equilibrium state and feedbacks

The budget analyses of FH13 showed that in the MIZ during quasi equilibrium three approximate balance conditions were met: 1) buoyancy, the positive buoyancy flux associated with the release of low-salinity meltwater was balanced by negative buoyancy fluxes from air–sea heat loss and the advective convergence of higher salinity waters; 2) energy, the reduction of mixed layer enthalpy owing to the convergence of ice mass was balanced by net advective and radiative ocean heat flux convergence, and 3) ice mass, the advective convergence of ice mass was balanced by thermodynamic melting. The establishment of these balances conditions in quasi-equilibrium suggests that *imbalances* in one or more of these terms may be important in the period preceding quasi equilibrium.

The MESEM may operate in the period preceding quasi equilibrium in the following manner. Unbalanced positive buoyancy forcing from low-salinity ice meltwater stabilizes the mixed layer. A more stable mixed layer disrupts the energy balance by reducing vertical ocean sensible heat flux convergence. Reduced ocean sensible heat flux convergence disrupts the ice mass balance by lowering seawater temperatures and sea ice basal melt rates. With reduced basal melt rates, more ice survives advection into and across the mixed layer. Ice surviving transport across the mixed layer may melt in waters beyond the MIZ. The release of meltwater beyond the MIZ disrupts the local buoyancy balance, restarting the MESEM. A summary of the novel positive-feedback MESEM hypothesis is summarized in Table 2.

TABLE 2. Summary of the meltwater stabilization enhancement mechanism (MESEM).

i.	Sea ice is advected into the MIZ or in the open ocean beyond the MIZ
ii.	The ocean loses heat and gains fresh ice meltwater, the net effect of which is to increase its buoyancy
iii.	The mixed layer shoals and becomes more stratified
iv.	The rate of advective ocean sensible heat flux convergence into the mixed layer falls with the suppression of convective mixing
v.	Temperatures in the mixed layer fall from ocean-ice and air-sea heat fluxes
vi.	The rate of ice mass convergence gradually exceeds the rate of ice melt
vii.	The MIZ and the region of balanced ice mass flux advances

The large discrepancy between the observed and predicted ice cover in the northern LS (section 3) suggests that the MESEM may be involved in the expansion of sea ice in that region. Hence, the following investigation of the MESEM focuses on the role of buoyancy forcing from sea ice–ocean interaction in the expansion of ice cover in the northern LS. The discussion is based on the coupled sea ice–ocean state estimate of the LB&BB constructed for the period 1996/97 and described in detail by FH13. Salient features of the state estimate are summarized in appendix B.

a. Analysis of the 1996/97 state estimate

The sea ice quasi-equilibrium period, the period of relative sea ice edge stability during which ice extent is maximum, is identified in the 1996/97 annual cycle between 21 February and 20 March. During quasi equilibrium, the total ice extent in the domain is $(1.3 \pm 0.05) \times 10^6$ km^2. During this time, the location of the MIZ is regularly displaced by synoptic winds, ocean eddies, current meanders, and other sea ice–ocean interactions due to the evolving ocean state. A sense of typical MIZ displacement during quasi equilibrium—an advance over the NS and retreat along the Labrador shelfbreak below 55°N—is provided in Fig. 4a.

Figure 4b shows that the ice edge advances far across the THF in the northeast Labrador Sea, or northeast corner (NEC), in the months preceding quasi equilibrium. Using the ice drift rates given by the state estimate and using the December ice edge as the starting point, we calculate that if ice advected south did not melt, the ice edge would surpass the observed maximum position

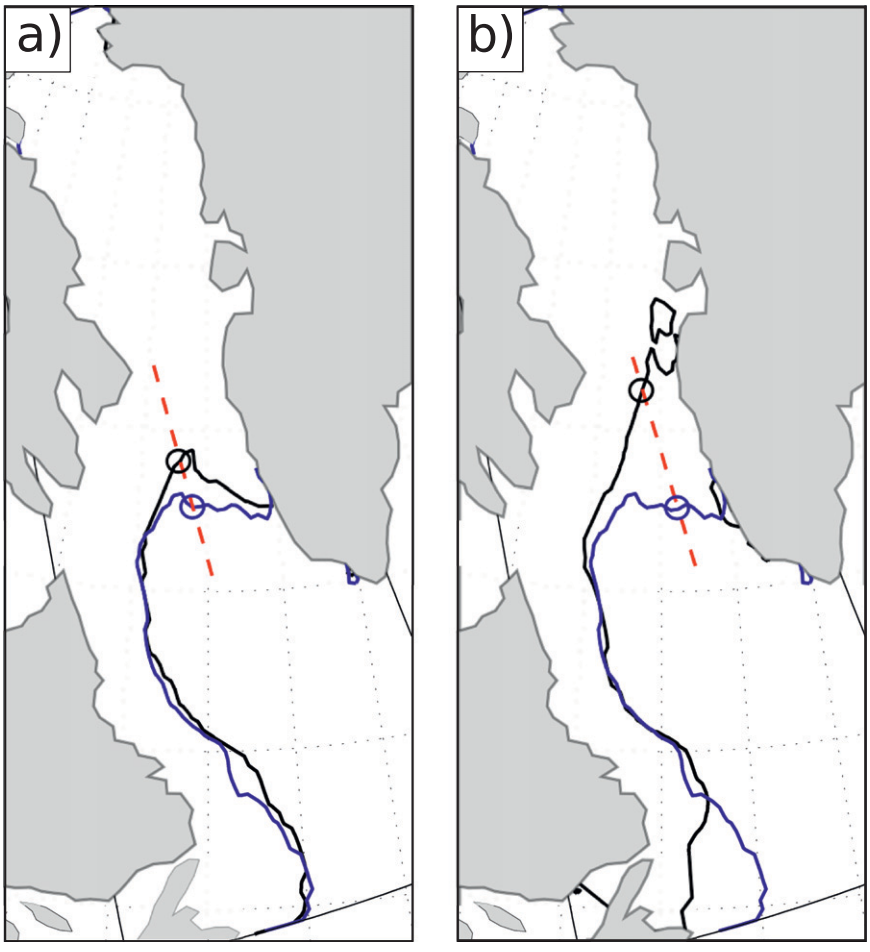

FIG. 4. Sea ice edge (the 15% ice concentration limit) advancement during two periods: (a) the quasi-equilibrium period (21 Feb–20 Mar) and (b) several weeks preceding the quasi-equilibrium period (30 Jan–20 Mar). Dashed lines indicate the cross section location used in Figs. 5 and 6. Circles indicate the ice edge location on the sections at the beginning and end of the periods.

by early February and continue several hundred kilometers farther south by mid-March.

Why is the greatest advance of the ice edge across the THF greatest in the NEC? Are there identifiable hydrographic differences in the NEC that allow the MESEM to operate? If so, hydrographic and sea ice extent variability may be more coupled than previously assumed.

To investigate the connection between hydrography and the MESEM, we examine the hydrographic developments during the ice edge advancement at two locations and times: the small advance over the NS during quasi equilibrium and the large advance in the NEC during the weeks leading up to quasi equilibrium.

1) NS

The sea ice and ocean states during two stages of quasi equilibrium are provided in Fig. 5. The mean state for the week ending 27 February (Fig. 5a) shows a warm (2°–5°C) subsurface IW core at 400 m, the ventilation of subsurface heat in convectively deepened mixed layers, cold highly stratified surface AW, and the THF identified in FH13. Also evident is a southward extension of anomalous cold, fresh highly stratified waters beyond the sea ice edge overlaying the warmer (>2°C) IW between 62.5° and 64°N. Exposure to air–sea buoyancy losses has deepened the mixed layer south of 64°N to between 50 and 500 m. Ventilation of IW occurs south of 62.5°N. To the north of 62.5°N and beneath some of the ice, IW is isolated from the surface at a depth of ~100 m.

Ice thickness along this section decreases from north to south from 1.1 to 0.4 m. Such a thinning pattern is consistent with ice volume divergence caused by an acceleration of ice in the along-section direction of ~25%. The ice edge is within 100 km of a sharp horizontal density gradient at 64.5°N which coincides with

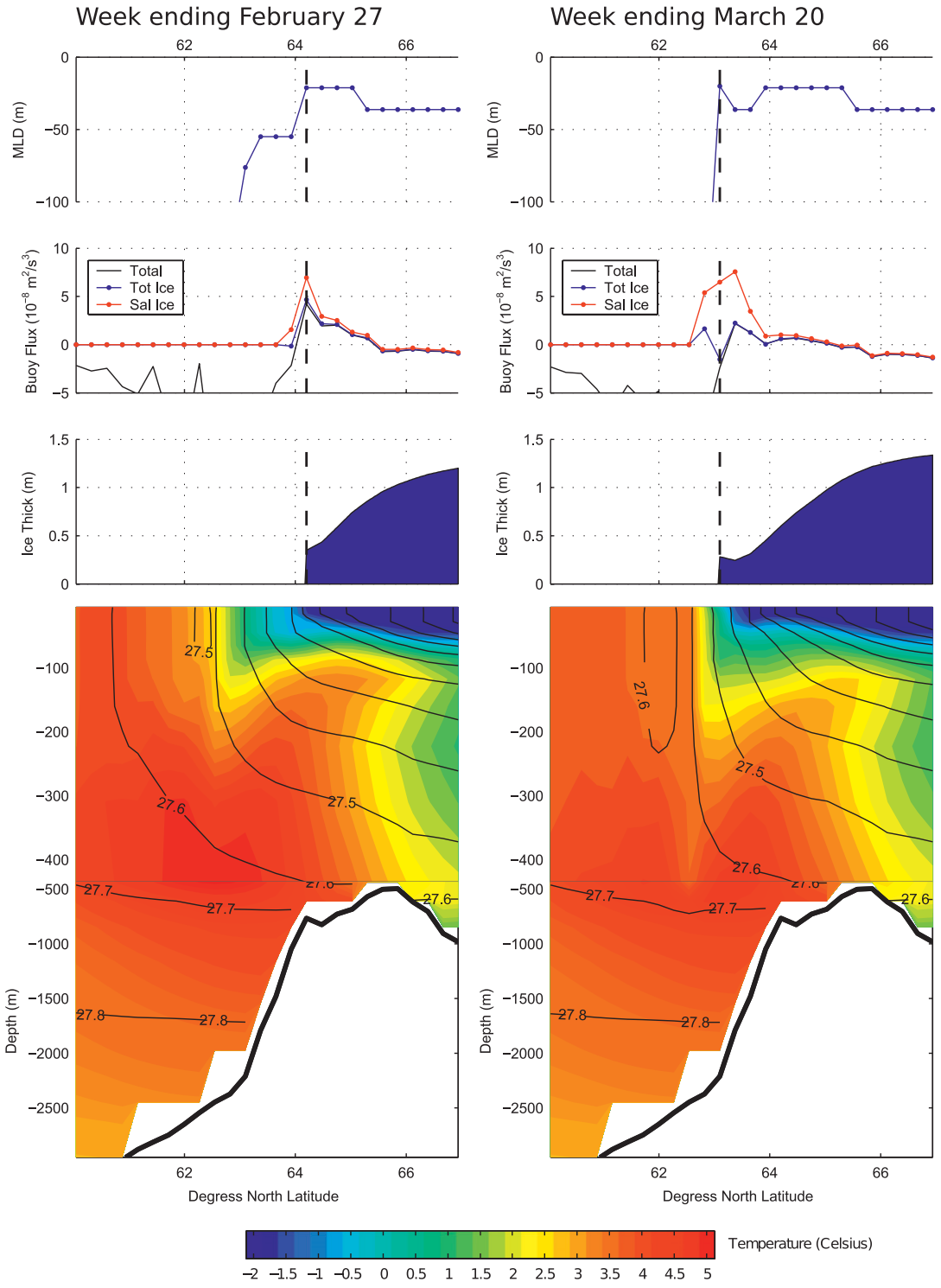

FIG. 5. Virtual hydrographic transects in the north-central Labrador Sea at the (left) beginning and (right) end of the quasi-equilibrium period. (top to bottom) Mixed layer depth (above 100 m); surface buoyancy flux (10^{-8} m^2 s^{-3}), ice thickness; and ocean temperature and surface-referenced potential density. Transect location indicated in Fig. 4a. Contributions to seawater surface buoyancy fluxes are decomposed as 1) ice processes altering S, 2) ice processes altering T and S, and 3) all processes altering T and S. Hydrography panels indicate T (shaded) and potential density isopycnals ($\sigma_0 - 1000$ kg m^{-3}) (contours). Vertical depth spacing increases below 500 m. Bathymetry is shown by heavy line. The sea ice edge, the 15% ice concentration limit, closely corresponds to the zero sea ice thickness limit.

the outcropping of the $\sigma_0 = 1027.1$ kg m^{-3} isopycnal – the THF.

The pattern of surface buoyancy forcing shows that sea ice processes alter ocean surface buoyancy in opposite senses to the north and south of 65.5°N. To the north, thermodynamic sea ice growth removes freshwater from the upper ocean thereby increasing its salinity and decreasing its buoyancy. To the south, sea ice melting decreases seawater salinity and removes sensible heat from the ocean mixed layer, the net effect of which is a buoyancy increase. Positive sea ice buoyancy fluxes peak at the ice edge, reflecting high ice melt rates in warmer offshore waters. The total ocean surface buoyancy forcing is almost completely dominated by ice–ocean interaction where ice is present. Beyond the MIZ, the total ocean surface buoyancy fluxes are large and negative primarily owing to intense air–sea heat losses. Finally, the mixed layer is shallow behind and MIZ, especially between 64° and 65°N, and progressively deepens to the south. Importantly, the mixed layer adjacent to the MIZ is shallower (~150 m) than the subsurface IW between 63° and 64°N,

Three weeks later, during the week of 20 March (Fig. 5b), significant changes are evident in the ice distribution, hydrographic structure, surface buoyancy forcing patterns, and mixed layer depths. The IW core at 400 m is 1.4°C cooler and upper-ocean temperatures beneath the expanded ice are cooler by 1.0°C–2.4°C. The warm IW core is vertically split with the dividing line falling close to the new ice edge.

The newly extended ice cover is quite thin (≤0.25 m) because of increased melting in the warmer waters to the south. The distance traversed by the ice edge during this time yields an effective mean velocity of 7.75 km day^{-1}. The actual mean velocity is about twice as fast, 15.45 km day^{-1}. The discrepancy between observed and actual velocities is explained by melting at advancing ice edge by sea ice–ocean heat fluxes.

The qualitative patterns of the ocean surface buoyancy fluxes remain the same. In the vicinity of the earlier MIZ, net ice-related buoyancy fluxes are near zero, indicating that ocean–ice heat fluxes have mainly ceased. At and around the new ice edge, the positive sea ice meltwater buoyancy forcing term is larger than at the earlier ice edge despite thinner ice and nearly identical ice velocities (within 5%) reflecting the greater buoyancy increase from ice meltwater in higher salinity seawater. Nevertheless, the total ocean surface buoyancy forcing beyond the MIZ is negative—much more so than at the earlier ice edge. Finally, the mixed layer between the earlier and new ice edge locations is much shallower and horizontal mixed layer depth gradient across the ice-free and ice-covered regions is much greater.

The positive surface buoyancy forcing at the 27 February edge of the MIZ appears to contribute to the isolation of subsurface IW via mixed layer shoaling and stabilization enhancement. The observation of substantial meltwater release to the south of the actual ice edge supports this interpretation.

The state estimate suggests that the efficiency of the MESEM may be limited to regions with special upper-ocean hydrographic properties. During the week of 27 February, isopycnal slopes indicate IW ventilation in waters denser than 1027.5 kg m^{-3}. To the north, between the 1027.0 and 1027.5 kg m^{-3} isopycnal outcroppings, the upper (~100 m) of the ocean is comparatively cooler, fresher, and more stratified. These waters are modified IW: fresher than IW and saltier than AW and sea ice meltwater.

Three scenarios are conceivable for the failure of the ice edge to advance across waters that are mixing with subsurface IW: (i) when the ice edge is adjacent to warm salty surface waters, the buoyancy gain from meltwater release may not be sufficient to offset the buoyancy loss from air–sea heat loss and the advective convergence of higher salinity waters; (ii) the seasonal increase of solar radiation may instigate melting before the meltwater can sufficiently increase the seawater buoyancy; and (iii) ocean sensible heat flux from lateral advection may be sufficient to melt all incoming ice independent of upper-ocean stratification. The question of ice advancement across the THF is further investigated in section 4b. We now turn to the NEC.

2) NEC

In section 3 we showed that the area of largest discrepancy between the state estimate and the 1D model is the NEC, north of 62.5°N. The ice edge predicted by the 1D models closely traces the location of the THF. The NEC coincides with a second source of AW in the model domain, the WGC. The result of the previous section that the distribution of modified IW may be related to the quasi-equilibrium sea ice location suggests that the upper-ocean hydrographic conditions in the NEC share characteristics with waters above the central Northern Slope.

Cross sections from the state estimate along the transect shown in Fig. 4b are presented in Fig. 6. The two selected seven-day mean states correspond to the ice pack's crossing of the THF at January's end and the maximum ice extent realized in mid-March. Qualitatively, they share many features with the cross sections described in Fig. 5. A warm salty IW core is identified, which becomes progressively cooler as it ventilates. An area of low-salinity modified IW is identifiable in the upper 100 m between the initial and final ice edge positions. North of 63.75°N, subsurface IW beneath the

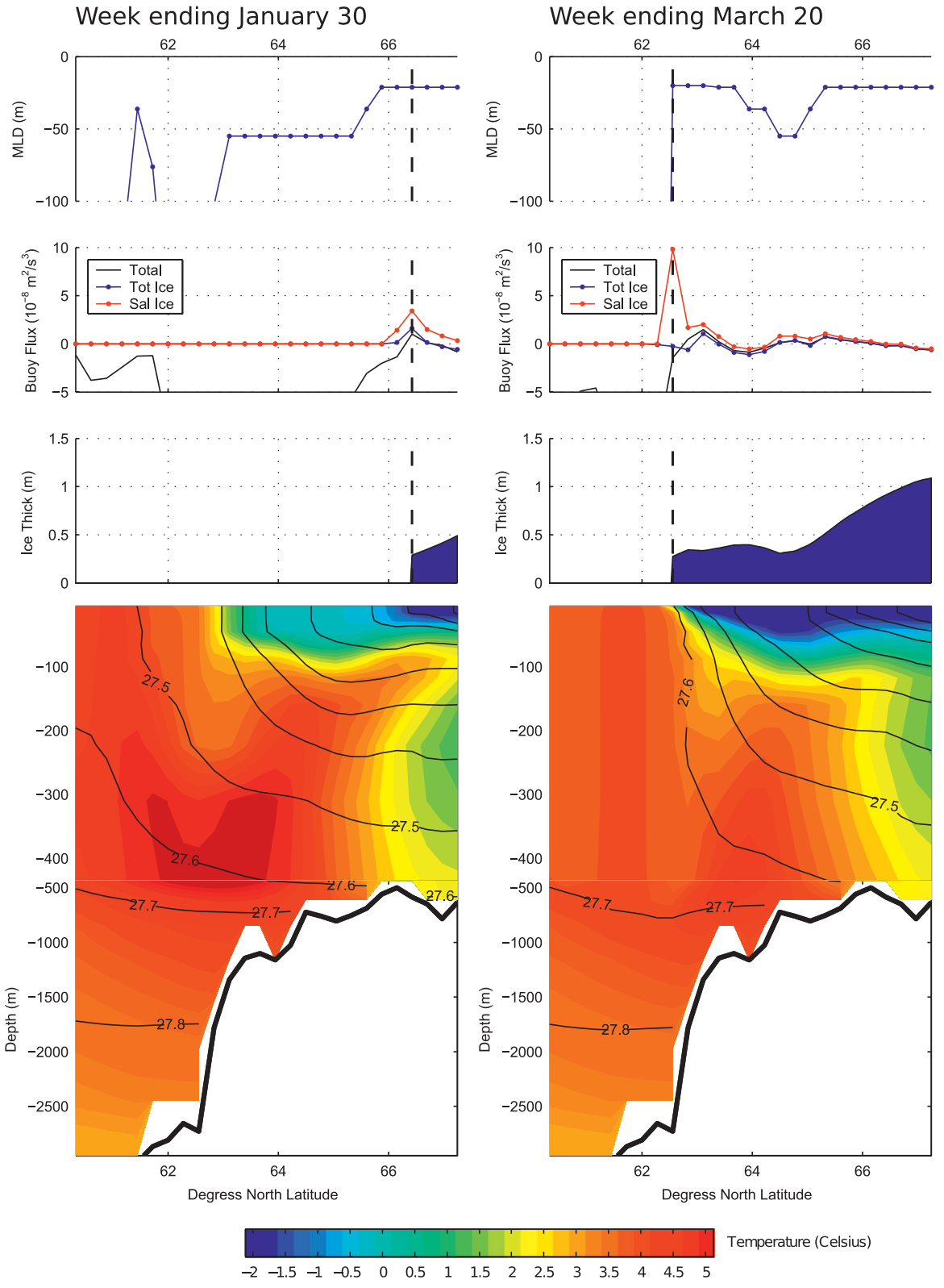

FIG. 6. As in Fig. 5, but for (left) 30 January 30 and (right) 20 March 20 along the hydrographic section indicated by Fig. 4b.

low-salinity modified IW remain isolated from the surface. Initially low rates of meltwater buoyancy flux at the ice edge become substantially greater when the ice meets mixed layer–entrained IW at 62.5°N. The mixed layer shoals or remains at the same depth along the entire length of ice advancement.

The ice thickness profiles of Fig. 6b reveal uniformly thin (≤0.5 m) ice along the entire length of ice advancement across the THF, which warrants an explanation. At ~64°N net ice buoyancy fluxes are negative, the mixed layer is relatively deep, and the ice is somewhat thicker than to the north and south. Net negative sea ice–related buoyancy fluxes indicate thermodynamic ice growth. This implies that while large amounts of ice may need to melt to stabilize the upper ocean, once stabilized and ice covered, nothing prevents thermodynamic growth. However, when the stabilization is marginal, as is the case here, ice growth may be limited by a negative feedback process wherein the negative seawater buoyancy flux associated with the ice thickening may trigger subsurface heat ventilation, which leads to ice melt. The operation of the negative feedback keeps ice thickness below 0.5 m in the region between 62.5° and 65.0°N despite large air–sea ice heat fluxes (not shown). Indeed, during quasi equilibrium, net ice–related buoyancy fluxes are near zero in the NEC, indicating a cancellation of buoyancy fluxes: negative from ice growth/high-salinity brine release; positive from ice melt/low-salinity brine release. Because of the marginal stability of the mixed layer along the entire length of the near-surface modified IW, sea ice thicknesses beyond the THF remain thin.

3) Sea ice and hydrographic evolution

An overall interpretation of the sea ice and hydrographic evolution in both regions is now possible. An expanse of modified (fresher, cooler, and more stratified) IW overlays some of the warmer subsurface IW south of the THF. Melting ice progressively shoals the mixed layer in the MIZ before mixed layer deepening can entrain subsurface IW. The operation of the MESEM is associated with the translation of the ice edge in the direction of offshore ice drift on the IW side of the THF. Once the MIZ is adjacent to waters mixed with ventilated IW, progressive ice drift out of the MIZ leads to extremely high melt rates. The MIZ advancement beyond the THF is observed only over specific hydrographic conditions—comparatively cold fresh and stratified waters (to ~125 m) overlaying the warm salty weakly stratified IW below. In the hydrographic regime of surface-mixed IW the MESEM does not operate (the mixed layer does not appreciably shoal and the MIZ location is stationary) for reasons that are not yet obvious. The waters satisfying the specific hydrographic conditions are presently termed SIPW.[1] We have conducted similar analyses for several additional transects across the NS. All such transects are fundamentally similar.

b. Importance of the MESEM

In demonstrating the importance of the MESEM, one issue is whether sea ice advection alone (instead of the MESEM) may account for the quasi-equilibrium ice edge position. For example, the 1D thermodynamic ice-growth model may have failed to predict ice on the IW side of the THF simply because lateral transports of ice are required to cool upper ocean temperatures to the point where ocean–ice heat fluxes are too feeble to melt all advective-converging ice in the MIZ. If so, sea ice–related surface buoyancy forcing would play no role in the presence of ice on the IW-side of the THF. Discerning the regions where the MESEM is relevant for the development of the sea ice quasi-equilibrium state can be determined with a simple model experiment.

1) Experimental setup

The sea ice model is altered so as to eliminate the positive buoyancy forcing associated with the release of ice meltwater. The regions where the MESEM feedback are important are revealed by examining the different ice pack distributions in the state estimate and the experiment. To eliminate the MESEM, the sea ice meltwater salinity in the model is instantaneously equated with the salinity of the upper-ocean grid cell into which it is released. With this modification, sea ice can only reduce ocean surface buoyancy—increasing salinity during thermodynamic growth and decreasing temperatures during ocean–ice heat fluxes.

The numerical model is initialized and forced using the same adjusted fields which generated the state estimate. As the atmosphere is noninteractive, mismatches between the prognostic sea ice–ocean state and the prescribed atmospheric state are inevitable.[2] Therefore, the

[1] The use of the word *preconditioned* used here should not be confused with a distinct usage pertaining to deep convection proclivity in the Labrador Sea. Examples of the use of the term *preconditioning* or *preconditioned* to refer to a low-salinity ocean state favorable to sea ice can be found in McPhee et al. (1987) and Kitoh et al. (2001).

[2] For example, surface air temperatures over sea ice tend to be lower than over open water. In the areas of sea ice area discrepancy between the state estimate and the experiment, surface air temperatures may be inconsistent with the ocean state (Griffies et al. 2009). The prescribed surface air temperatures bring with them an imprint of the "true" ice extent. Consequently, where ice is present in the state estimate but absent in the experiment, the surface air temperatures will be consistent with an ice-covered state and therefore be colder than they would be over open water.

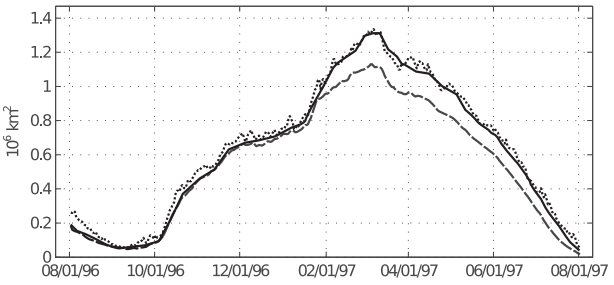

FIG. 7. Total sea ice area from 1 Aug 1996 in the study region from observations (dotted), the optimized state estimate (solid), and the MESEM-OFF experiment (dashed).

results of this experiment should not be interpreted as a prediction of the coupled ice–ocean–atmosphere system evolution without MESEM, but merely as providing an indication of where MESEM may be important.

2) EXPERIMENT RESULTS

We compare the results from the 1-yr simulation without MESEM (MESEM-OFF) with those from the original state estimate (MESEM-ON) and with observations in three ways: 1) time series of total daily ice area over the annual cycle, 2) sea ice concentration field during the quasi-equilibrium period, and 3) two sea ice–ocean transects.

The time series of total sea ice area in the domain with MESEM-OFF differs from the observations (and MESEM-ON), as shown in Fig. 7. During the initial freeze up of the Baffin Bay and northern Labrador Shelf (until mid-January) the total ice area of MESEM-OFF tracks closely with observations in agreement with the 1D model, albeit with a slight negative bias ($\sim 0.1 \times 10^6$ km^2).

The negative bias in the MESEM-OFF total ice area grows from mid-January, coinciding with the time when ice is observed to cross the THF in the southeastern Baffin Bay and offshore from the inner Labrador Shelf across the shelfbreak. From February to mid-March, the expansion of total ice area in MESEM-OFF grows less than observed. Both MESEM-OFF and observations attain seasonal sea ice maximum extent at approximately the same time. After the peak in total ice area, ice area loss in MESEM-OFF proceeds at a slightly slower rate than observations.

From the above, the MESEM does indeed appear to be important for the development of sea ice across the Labrador Shelf and across the THF in the Labrador Sea. To determine where the discrepancy between the observed and MESEM-OFF simulated total sea ice area is largest, we analyze the spatial patterns of ice concentration in MESEM-OFF in Fig. 8.

Virtually no ice is found across the THF in MESEM-OFF with the exception of a small ice patch in the NEC near the WGC bifurcation. The NEC ice patch suggests that the lateral transport of AW and ice from the inner shelf component of the WGC can be important for the development of some ice in northern Labrador Sea.

To gain further insight into the relation between the ice edge and the IW waters, Fig. 9 presents sea ice–ocean cross sections along the same two transects defined in Figs. 4a and 4b during quasi equilibrium.

Without the MESEM, the ocean states along these two transects evolve along different lines but share several common features. First, in MESEM-OFF the ventilation of subsurface IW during quasi equilibrium occurs at approximately the same location as MESEM-ON despite a MIZ found farther north. Second, the SIPW mixed layer, the mixed layer of waters between the IW ventilation area and the MESEM-OFF MIZ, are deeper in MESEM-OFF, but not so deep as to entrain subsurface IW. Third, without sea ice to insulate and mitigate air–sea heat fluxes, the temperatures in the deeper SIPW mixed layer are colder in MESEM-OFF, but remain above the freezing point.

The ice-free SIPW in MESEM-OFF are subject to large heat losses to the atmosphere from air fluxes and to sea ice advected across the THF from ocean–ice fluxes (see Fig. 9 of FH13). It is easy to imagine that the subsurface IW is the source of the enthalpy required to keep the SIPW ice free in the face of such large sustained wintertime heat losses. However, from the transects it is clear that the SIPW stratification is sufficient to prevent the entrainment of subsurface IW into its mixed layer. As the SIPW mixed layer cannot tap the reservoir of subsurface IW enthalpy, its temperature falls toward, but does not reach, the freezing point. In contrast, the temperatures of the mixed layers entraining subsurface IW remain relatively warm, above 2.5°C.

Hence, from these transects two features of SIPW are identified. One, the initial enthalpy of SIPW is sufficient to prevent both the local thermodynamic production of sea ice and the accumulation of ice advected across the THF. Two, initial stratification of SIPW prevents the convective entrainment of subsurface IW thereby allowing the SIPW temperatures to cool toward the freezing point.

The inability of the ice advected across the THF in MESEM-OFF to advance across the SIPW suggests that the operation of the MESEM is more sensitive to net ocean surface buoyancy fluxes than to sea ice melt rates. Indeed, the colocation of the MIZ and the IW ventilation site in MESEM-ON is probably not due to the presence of the warm IW-infused mixed layer as all ice advected across the THF in MESEM-OFF melts farther

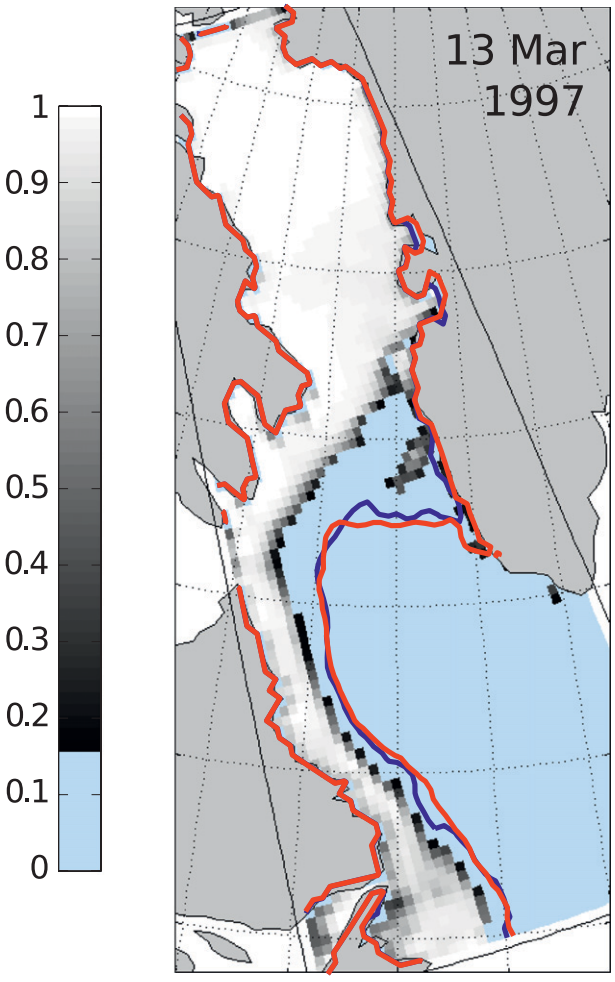

FIG. 8. Mean sea ice concentration [(0−100%)/100%] during quasi-equilibrium (week ending 13 Mar) from the MESEM-OFF experiment (colors) and the sea ice edge [15% (0.15) concentration cutoff] from observations (red line) and the state estimate (blue line).

north despite much colder SIPW mixed layer temperatures. Ocean surface buoyancy losses due to air–sea and ocean–ice heat fluxes in the comparatively warm IW-infused mixed layers are expected to be greater than in the comparatively cold SIPW mixed layers. It is possible, therefore, that the operation of the MESEM is limited to SIPW because it is only in SIPW that the release of sea ice meltwater can change the net ocean surface buoyancy fluxes from negative to positive. With a net positive ocean surface buoyancy flux, the MESEM can proceed beyond step II described in Table 2.

c. Characterization of sea ice–preconditioned waters

The hydrographic properties of the SIPW amenable to the MESEM in the Northern Slope of the Labrador Sea are now characterized.

1) IDENTIFICATION AND SPATIAL PATTERNS

A simple method is used for identifying sea ice–preconditioned waters: as the sea ice concentration fields from the MESEM-OFF experiment place the MIZ along the approximate location of the THF, we can tentatively identify SIPW as being upper-ocean waters on the IW side of the THF over which sea ice spreads at some point in the sea ice annual cycle. The THF position in the 1996/97 state estimate is also recognized as the southernmost extent of sea ice during the week of 4 December 4 (see appendix A).

A sense of the spatial variations of the SIPW properties in the upper 20 m (top two model levels) from the state estimate is provided in Fig. 10. By 4 December the seasonal thermocline has been eroded, revealing the domain's distinct near-surface water mass types: IW in the central Labrador Sea ($S \geq 34.5$) and AW on the Baffin Bay and along the Labrador Shelf ($S \leq 33.25$). The SIPW have temperatures, salinities, and potential densities of intermediate values between the IW and AW, consistent with the findings of the state estimate hydrographic cross-section analyses.

The hydrographic properties of the SIPW are spatially variable in December and March with the lowest values near Disko Bay and generally increasing values to the south. SIPW spatial heterogeneity persists during quasi equilibrium, although the salinity variations in the later period are smaller.

2) *T–S* DIAGRAMS

The evolution of the water mass properties in the surface (upper 20 m) and subsurface (310 m) within the box defined in Fig. 10a are presented as temperature–salinity (T–S) diagrams during four weeks preceding and during the sea ice quasi-equilibrium state in Fig. 11.

During the week ending 23 October (Fig. 11a), the near surface SIPW fall along a water mass property continuum between waters to the north (N-SIPW) and south (S-SIPW) with surface waters generally become warmer and saltier to the south (see appendix A for more details about the identification of N- and S-SIPW). At the lowest latitudes, the S-SIPW T–S points are clustered around $T = 4.5$°C and $S = 34.25$, consistent with the values found on the spatial maps in Fig. 10. At 310 m, the T–S range for all three regions is much narrower ($34 \leq S \leq 35$, 0°C $\leq T \leq$ 5.25°C) and lie along or close to the $\sigma_0 = 1027.5$ kg m^{-3} isopycnal.

An important feature of low-salinity N-SIPW and SIPW is identified in the 23 October T–S diagram: the N-SIPW and SIPW remain less dense than the waters below them at 310 given arbitrary temperature reductions. In contrast, temperature reductions of S-SIPW

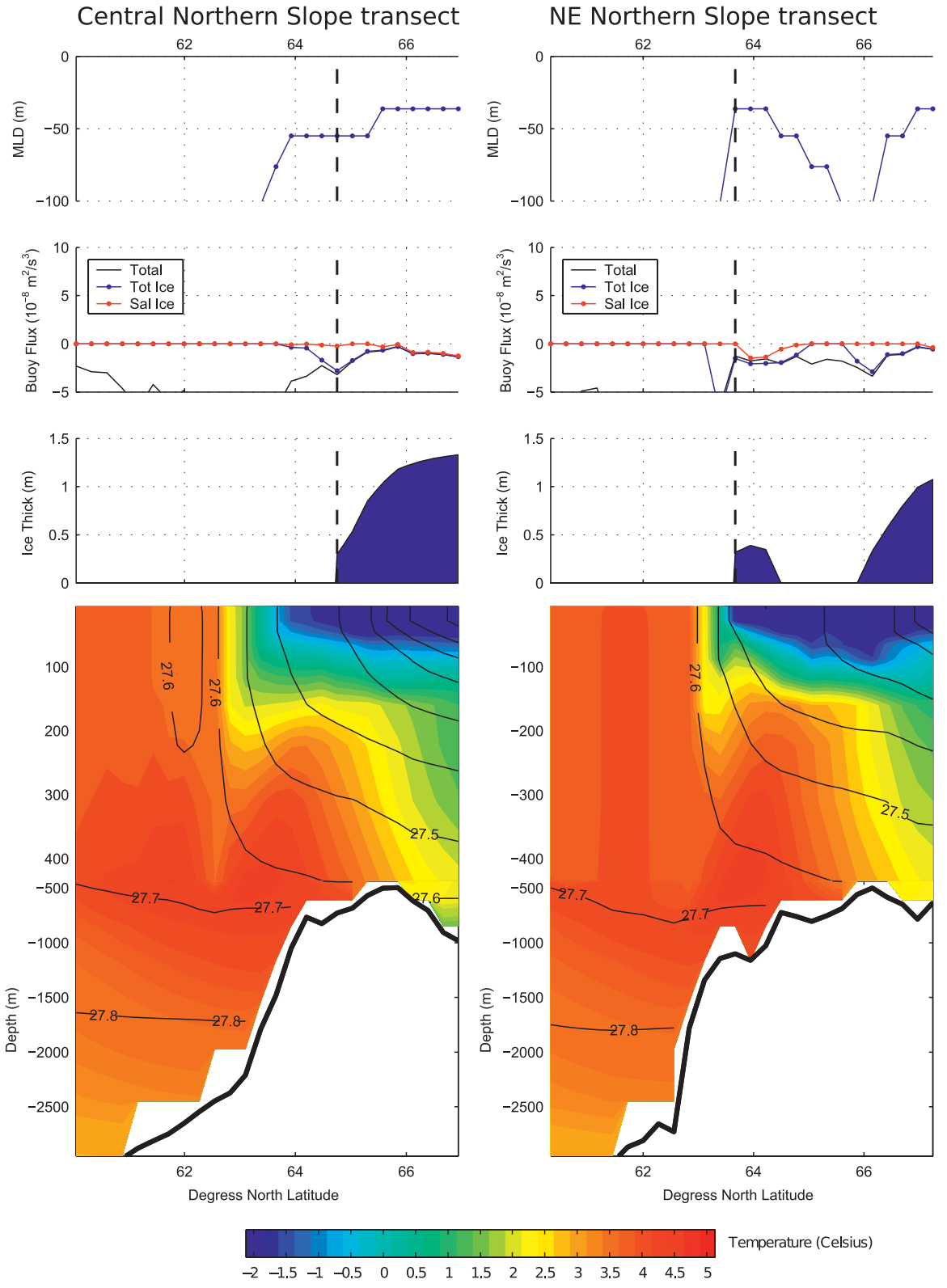

FIG. 9. MESEM-OFF sea ice and ocean state for the week ending 20 March across transects in the (left) central and (right) northeastern Northern Slope. The cross sections should be compared to those for MESEM-ON: left panel with Fig. 5b and right panel with 6b. Cross-section tracks are in the same locations as shown in Fig. 4.

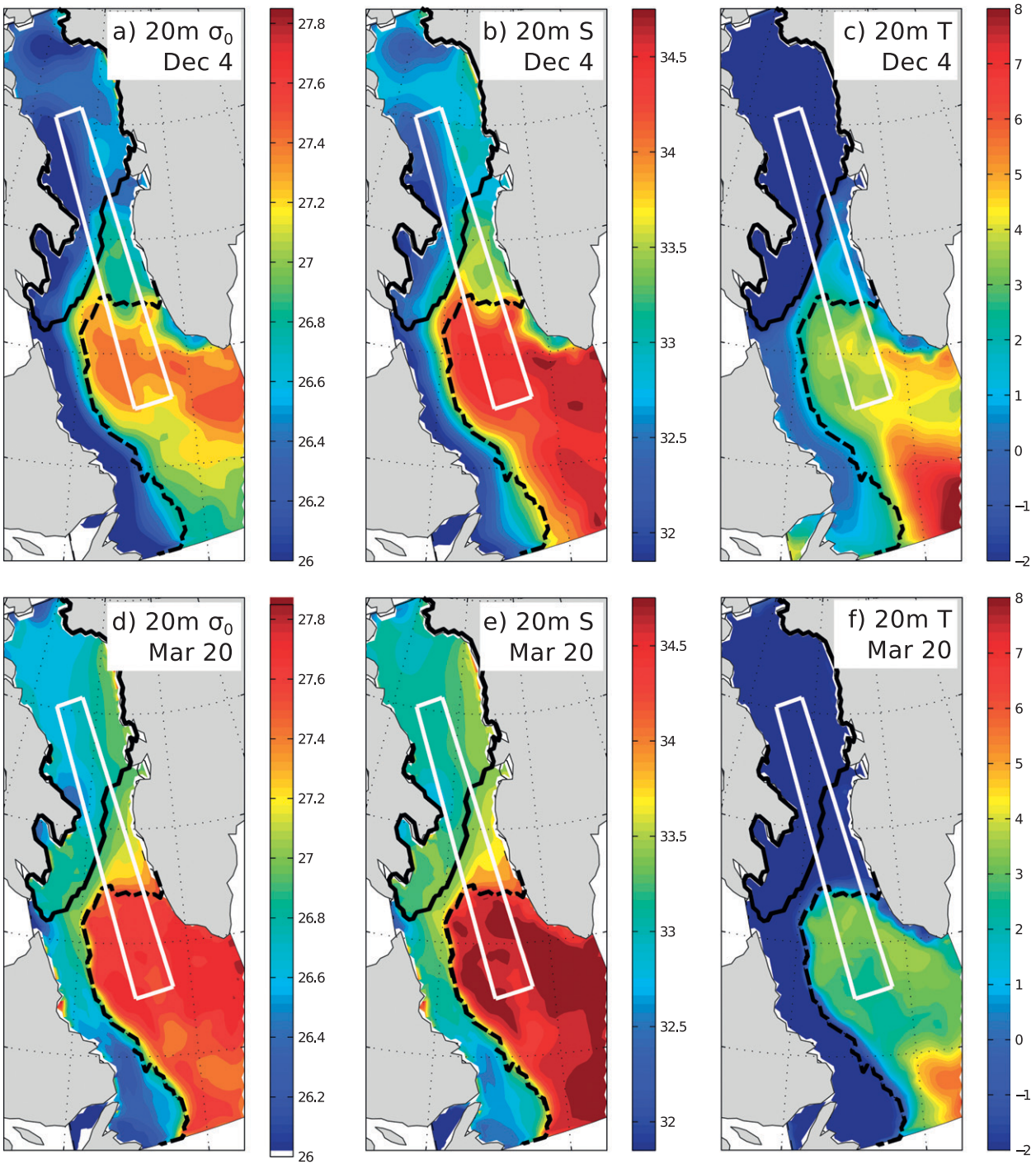

FIG. 10. Upper 20 m (a) potential density ($\sigma_0 - 1000$ kg m^{-3}), (b) salinity, and (c) temperature (°C) for week ending 4 Dec 1996. (d)–(f) As in (a)–(c), but for week ending 20 Mar 1997. Solid and dashed black lines denote 4 Dec and 20 Mar ice edge positions, respectively. White rectangles denote regions in region where water masses are characterized in Fig. 11.

will cause its density to *exceed or equal* the densities of the warm salty waters below.

From the MESEM-OFF experiments it was observed that the mixed layers in the SIPW never entrained subsurface IW. However, given a sufficiently long period of buoyancy loss it is possible that a progressively deepening mixed layer could eventually entrain IW before the mixed layer reached the freezing point.

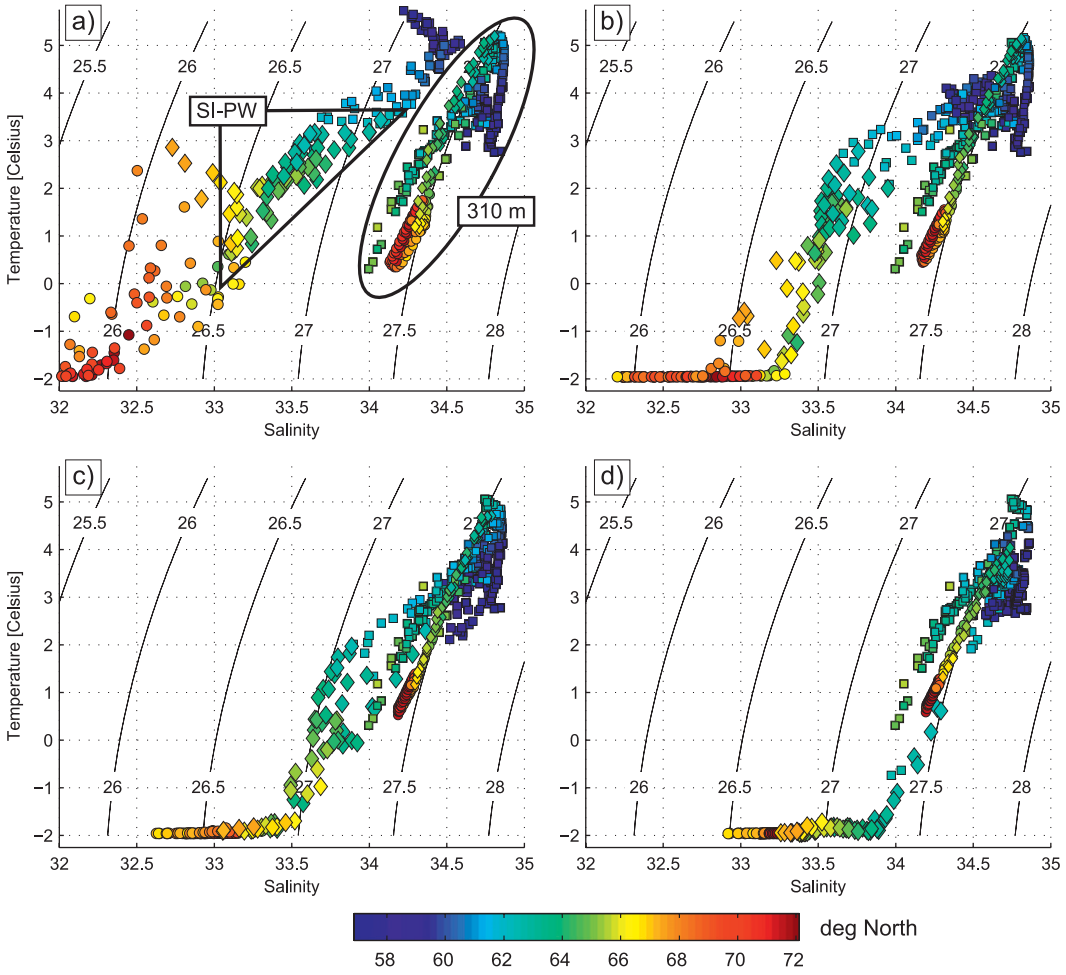

FIG. 11. The *T*–*S* diagrams for four one-week periods: (a) 23 Oct, (b) 4 Dec, (c) 29 Jan, and (d) 20 Mar. The *T*–*S* points 20 and 310 m within the domain are defined in Fig. 10a. Potential density ($\sigma_0 - 1000$ kg m^{-3}) is shown with contours. Colors denote the latitude of *T*–*S* points. Shapes identify period when sea ice appears in the 1996–97 annual cycle: circles (north of SIPW or N-SIPW), ice by 4 Dec; diamonds (SIPW), ice between 4 Dec and 20 Mar; squares (south of SIPW or S-SIPW) where ice never appears. In (a), triangle demarks sea ice–preconditioned waters, the oval demarks all subsurface waters; subsurface markers are smaller.

In contrast, surface waters in the S-SIPW region need not cool by more than a few degrees before warm subsurface IW are convectively entrained into the mixed layer.[3]

The evolution of the *T*–*S* diagrams between October and March supports the above interpretation. By 4 December, surface N-SIPW waters freeze (by construction), surface SIPW waters cool from north to south while remaining less dense than their subsurface counterparts, and surface S-SIPW waters begin to take on the *T*–*S* values of the waters below as they mix. By 20 March, S-SIPW waters have mixed with the waters below them as indicated by their cluster in *T*–*S* space. The salinity of N-SIPW increases owing to the several months of freshwater removal during thermodynamic ice growth. Finally, all surface *T*–*S* pairs of SIPW are at or near freezing (by construction) while maintaining distinctly lower densities from their subsurface counterparts.

SIPW can be characterized with a simple heuristic using the insights gained from the *T*–*S* diagram. A water parcel may be identified as sea ice preconditioned by determining whether it remains less dense than the IW below following an arbitrary temperature reduction.

[3] Recall that both the MESEM-OFF and 1D model experiments confirm that SIPW have enough sensible heat to resist freezing throughout winter and that it is only because of the MESEM that they eventually become ice covered.

In the 1996/97 annual cycle, SIPW may be identified for the week ending 4 December in terms of a salinity range:

$$33.1 \leq S \leq 34.10,$$

and a potential density range:

$$1026.6\,\mathrm{kg\,m^{-3}} \leq \sigma_0(T = -2°\mathrm{C}, S) \leq 1027.3\,\mathrm{kg\,m^{-3}}.$$

These ranges for identifying SIPW do not significantly change over several months before and during the sea ice quasi-equilibrium state.

The identification heuristic does not suggest that convective entrainment of IW is impossible within SIPW. Indeed, surface cooling and the progressive entrainment of saltier waters could increase SIPW density such that IW was entrained. Nevertheless, the mixed layers of SIPW identified with the above heuristic will almost always require more time to entrain IW and are expected to attain lower temperatures than the mixed layers of S-SIPW waters.

3) SIPW IN OTHER YEARS

It remains to be established whether the heuristic for SIPW realized in the 1996/97 annual cycle can be applied to other years. Analysis of the 1992/93 and 2003/04 state estimates reveals that sea ice cover variability across the THF is indeed limited to first order by the distribution of SIPW. The spatial distribution of the low-salinity upper-ocean anomalies and maximum sea ice edge locations for each of the state estimates is shown in Fig. 12.

Because of variability in the upper-ocean water mass properties (e.g., Yashayaev 2007) and strength of Labrador Current transport (Han et al. 2010) in the Labrador Sea between 1992 and 2004, the SIPW in each state estimate differ somewhat in terms of distribution and evolution in T–S space. Nevertheless, the correspondence of the distribution of low-salinity upper-ocean anomalies ($33 \leq S \leq 34$ at 20 m) and the maximum sea ice extent is unambiguous.

5. Discussion

The key finding of this work is that under certain hydrographic conditions the advancement of the marginal ice zone into the northern Labrador Sea requires a sea ice–ocean feedback process termed the meltwater stabilization enhancement mechanism (MESEM). In the MESEM, the release of buoyant sea ice meltwater in the marginal ice zone shoals and stabilizes the ocean mixed layer, eventually allowing the rates of advective ice convergence to exceed thermodynamic ice melt that leads to the gradual advancement of the MIZ into waters initially unfavorable for local thermodynamic growth.

The efficiency of the MESEM in advancing the ice edge is limited to certain hydrographic conditions: waters that are not actively mixing with warm salty subsurface subtropical-origin waters. These waters are found to have negative salinity anomalies in the upper 100 m and are termed sea ice-preconditioned waters (SIPW). The sea ice extent seaward of the Thermohaline Front is found to closely correspond to the extent of SIPW.

The positive buoyancy forcing associated with the ice meltwater release into the SIPW significantly reduces the depth of the ocean mixed layer ahead of the MIZ (not shown). Therefore, another important feature of SIPW is that they allow for the *accumulation* of meltwater ahead of the advancing ice front. The accumulation of meltwater ahead of the ice front enhances mixed layer stratification and suppresses vertical heat fluxes between the mixed and planetary boundary layers (not shown). With reduced mixed layer depths and vertical heat fluxes, ocean temperatures in the SIPW ahead of the MIZ fall faster than they would otherwise. With a sufficient reduction of mixed layer temperatures ahead of the MIZ, the rate of advective ice mass convergence can overcome the rate of thermodynamic melt allowing the ice edge to advance seaward.

The SIPW identification heuristic does not rule out the possibility of mixed layer deepening with arbitrary surface buoyancy losses. Indeed, the state estimates only show that the *rate* of mixed layer deepening is significantly reduced because of SIPW. Indeed, a preliminary analysis (not shown) of Argo T–S profiles from 1998 to 2012 recorded during autumn at locations across the Thermohaline Front that become ice covered during the following winter confirms the presence of negative upper-ocean salinity anomalies. Simple calculations show that the observed low-salinity waters will have more slowly deepening mixed layers and achieve lower minimum temperatures when subjected to realistic ocean surface heat fluxes than profiles taken just beyond the maximum ice edge in the central Labrador Sea.

A potential model bias in the relative importance of lateral heat fluxes to the MIZ by unresolved mesoscale eddies was also investigated, but not shown (see Fenty 2010). It was found that due to very small horizontal temperature gradients in the SIPW, the model's missing lateral eddy heat transport is probably important only for the maintenance of the sea ice edge during quasi equilibrium and not during the period of ice advancement across the Thermohaline Front.

Our findings have implications for the discussion of the sources of salinity anomalies in the subpolar North Atlantic and their role in setting wintertime ice extent

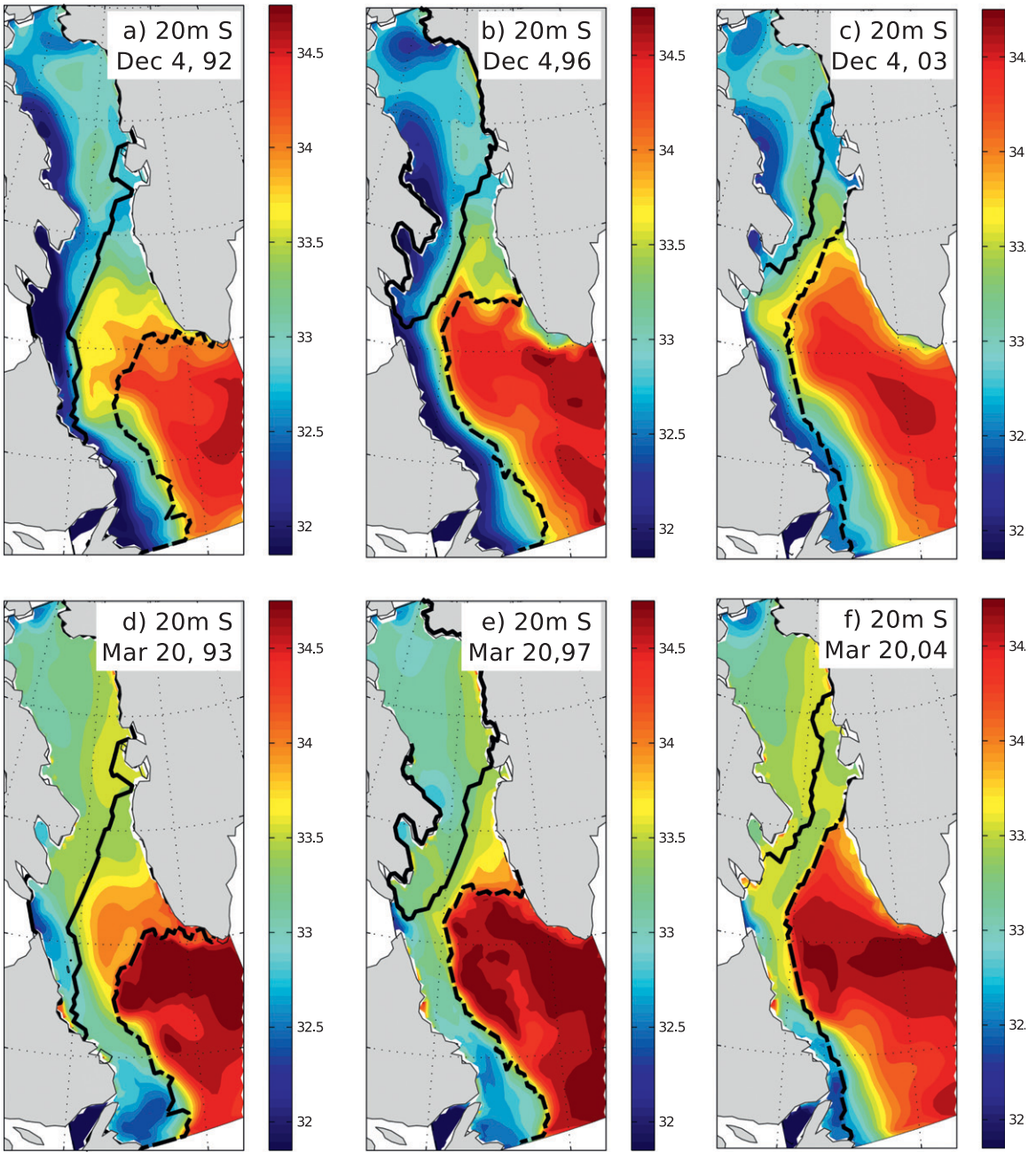

FIG. 12. Near surface (20 m) salinity for each of the three one-year state estimates 4 Dec (a) 1992, (b) 1996, (c) 2003, and 20 Mar (d) 1993, (e) 1997, and (f) 2004. Solid and dashed black lines denote the 4 Dec and 20 March ice edge positions, respectively. The pack ice advances across the THF (identifiable by the 4 Dec ice edge) and is ultimately arrested upon reaching the end of the SIPW—identified by the $S \approx 34$ isohaline in December. Waters with $S > 34$ are in communication with subsurface IW via convectively driven mixed layer entrainment. Note that the distribution and interannual variability of SIPW approximately follows the envelope between the 4 Dec and 19 March ice edge locations.

anomalies in the Labrador Sea. Ice extent–altering hydrographic anomalies have been recognized as potentially emerging from local interactions of the sea ice–ocean–atmosphere system. During periods of reduced deep convective mixing in the Labrador Sea, an unbalanced inflow of AW could lead to upper-ocean freshening (Houghton and Visbeck 2002). An enhancement of wintertime ice cover might be expected from this surface freshening until the return of deep convection removes the anomaly (Ikeda et al. 1996).

Several feedback loops link local sea ice anomalies in successive years. In this way, ice extent anomalies in one winter can alter the upper ocean hydrographic conditions for the next (Deser et al. 2002).

Even without an anomalous ice extent, the release of an anomalous quantity of ice meltwater following a year with higher than normal ice volumes could generate a surface freshwater anomaly. Because sea ice in the Labrador Sea and Baffin Bay can be transported several hundred kilometers over the course of a winter, the release of low-salinity meltwater can occur far from the site of ice growth. The enhanced surface stratification associated with anomalous ice meltwater release may persist through succeeding winters with obvious consequences for ice development (Belkin et al. 1998).

The described mechanism, if confirmed, would have implications for our ability to predict elements of sea ice evolution. Sustained hydrographic observations will be required to further elucidate the mechanisms controlling the origin and distribution of upper ocean salinity anomalies and their interplay with observed sea ice variability in the northwest North Atlantic.

Acknowledgments. The authors would like to acknowledge Carl Wunsch for providing valuable guidance during the course of this research and the preparation of the final manuscript. This research was carried out in part by an appointment to the NASA Postdoctoral Program at the Jet Propulsion Laboratory, California Institute of Technology, administered by Oak Ridge Associated Universities through a contract with NASA and in part through NSF Grant ARC-1023499, NASA's MAP Grant NNX11AQ12G, and the ECCO-GODAE project. We thank our ECCO-GODAE partners, the MITgcm development group, and the various data centers for making their data available.

APPENDIX A

SIPW Selection Details

The reason for using the 4 December ice edge location to identify SIPW is that the ice edge reaches this location in mid-November and subsequently remains stationary over a period of several weeks. It is only after a prolonged period of cooling and hydrographic modification by the MESEM that the ice advances further. The use of either the early December ice edge or the 33.25 isohaline at 15 m (the method used in FH13) gives nearly identical results. Furthermore, the 4 December ice edge location criteria is used to define the N-SIPW, PW, and S-SIPW regions to classify waters in the 23 October *T*–*S* diagram.

The 310-m depth level used to show subsurface *T*–*S* properties corresponds to the annual mean depth of the $\sigma_0 = 1027.5$ kg m^{-3} isopycnal, an isopycnal that outcrops along the MIZ around the time of the maximum wintertime sea ice extent.

The *T*–*S* pairs are given one of three categories: north of SIPW (N-SIPW) where ice is found by December 4, SIPW where ice forms between 4 December and 20 March, and south of SIPW (S-SIPW) where ice does not form by 20 March.

APPENDIX B

The Coupled Sea Ice–Ocean State of the LS&BB

The regional estimate of the coupled sea ice–ocean state in the LS&BB has been obtained through synthesis of satellite and in situ observations of sea ice and hydrographic properties available during the period 1996/97. The synthesis is based on the methodology developed by the consortium for Estimating the Circulation and Climate of the Ocean (ECCO). It is obtained via a gradient-based least squares fit of the Massachusetts Institute of Technology general circulation model (MITgcm) (Marshall et al. 1997a,b) to the data. The required gradient was calculated via the adjoint of the coupled sea ice–ocean model (Wunsch 2006; Wunsch and Heimbach 2007). Independent (control) variables that are subject to adjustment are three-dimensional fields of initial temperature and salinity, as well as time-varying two-dimensional fields of atmospheric state variables. Adjusted fields are allowed to vary within prior uncertainty estimates. First guess atmospheric forcing fields are from the National Centers for Environmental Prediction (NCEP)–National Center for Atmospheric Research (NCAR) reanalysis product (Kalnay et al. 1996). The fluxes are computed with the bulk parameterization of Large and Yeager (2004) and a parameterization for the melting of falling snow of Sathiyamoorthy and Moore (2002). The model has a $\frac{1}{3}^\circ$ horizontal resolution and 23 z levels. The sea ice model consists of a thermodynamic and dynamical component. It is described in detail in Menemenlis et al. (2005) and Losch et al. (2010). The adjoint of the coupled sea ice–ocean model was obtained via algorithmic differentiation (AD) (Heimbach et al. 2005) using the AD tool Transformation of Algorithms in FORTRAN (TAF) (Giering et al. 2005). It is an evolved form of the forward and adjoint model used in the sensitivity study of sea ice export through the Canadian Arctic Archipelago by (Heimbach et al. 2010). Dirichlet boundary conditions of temperature, salinity, and velocity are prescribed along the lateral ocean open boundaries following Ayoub (2006).

The present configuration possesses northern, eastern, and southern open boundaries.

In situ hydrographic observations are drawn from CTDs, autonomous profiling floats, and expendable bathythermographs (XBT). These data are compiled from the Hydrobase 2 of Curry (2001) and the Global Temperature and Salinity Profile Program from the National Oceanographic Data Center Operational Oceanography Group (2008) and include AR7W World Ocean Circulation Experiment (WOCE)-line cruises and measurements from the 1996/97 Labrador Sea Experiment. Daily satellite retrievals of sea ice concentration were obtained from the Comiso (2008) product, provided by the National Snow and Ice Data Center (NSIDC).

Of importance for the present study, the state estimate reproduces the spatial patterns and domain integrals of observed ice concentrations. In particular, the timing of ice advance and retreat, and the position of the sea ice edge are both accurately represented. The fidelity of the reproduction of the ice concentration evolution exceeds all known extant (dynamically consistent or otherwise) reproductions in the literature for this domain and time period. A detailed analysis is given in FH13.

REFERENCES

Ayoub, N., 2006: Estimation of boundary values in a North Atlantic circulation model using an adjoint method. *Ocean Modell.,* **12** (3–4), 319–347, doi:10.1016/j.ocemod.2005.06.003.

Belkin, I., S. Levitus, J. Antonov, and S. Malmberg, 1998: ''Great Salinity Anomalies'' in the North Atlantic. *Prog. Oceanogr.,* **41,** 1–68.

Carsey, F. D., B. Holt, S. A. D. Argus, M. J. Collins, C. E. Livingstone, and C. Tang, 1989: Overview of LIMEX'87 ice observations. *IEEE Trans. Geosci. Remote Sens.,* **27,** 468–482.

Comiso, J., cited 2008: Bootstrap Sea Ice Concentrations from Nimbus-7 SMMR and DMSP SSM/I-SSMIS, [01 August 1992 to 01 August 2004]. National Snow and Ice Data Center, Boulder, CO, digital media. [Available online at http://nsidc.org/data/docs/daac/nsidc0079_bootstrap_seaice.gd.html.]

——, and F. Nishio, 2008: Trends in the sea ice cover using enhanced and compatible AMSR-E, SSM/I, and SMMR data. *J. Geophys. Res.,* **113,** C02S07, doi:10.1029/2007JC004257.

Curry, R., 2001: Hydrobase 2—A database of hydrographic profiles and tools for climatological analysis. Woods Hole Oceanographic Institution Tech. Reference Preliminary Draft, 81 pp.

DeGrandpre, M. D., A. Koertzinger, U. Send, D. W. R. Wallace, and R. G. J. Bellerby, 2006: Uptake and sequestration of atmospheric CO_2 in the Labrador Sea deep convection region. *Geophys. Res. Lett.,* **33,** L21S03, doi:10.1029/2006GL026881.

Deser, C., and H. Teng, 2008: Evolution of Arctic sea ice concentration trends and the role of atmospheric circulation forcing, 1979-2007. *Geophys. Res. Lett.,* **35,** L02504, doi:10.1029/2007GL032023.

——, M. Holland, G. Reverdin, and M. Timlin, 2002: Decadal variations in Labrador Sea ice cover and North Atlantic sea surface temperatures. *J. Geophys. Res.,* **107** (C5), doi:10.1029/2000JC000683.

——, G. Magnusdottir, R. Saravanan, and A. Phillips, 2004: The effects of North Atlantic SST and sea ice anomalies on the winter circulation in CCM3. Part II: Direct and indirect components of the response. *J. Climate,* **17,** 877–889.

Fenty, I. G., 2010: State estimation of the Labrador Sea with a coupled sea ice-ocean adjoint model. Ph.D. thesis, Massachusetts Institute of Technology, 277 pp.

——, and P. Heimbach, 2013: Coupled sea ice–ocean-state estimation in the Labrador Sea and Baffin Bay. *J. Phys. Oceanogr.,* **43,** 884–904.

Giering, R., T. Kaminski, and T. Slawig, 2005: Generating efficient derivative code with TAF: Adjoint and tangent linear euler flow around an airfoil. *Future Gener. Comput. Syst.,* **21,** 1345–1355.

Griffies, S. M., and Coauthors, 2009: Coordinated Ocean-Ice Reference Experiments (COREs). *Ocean Modell.,* **26** (1–2), 1–46.

Häkkinen, S., and P. Rhines, 2004: Decline of subpolar North Atlantic circulation during the 1990s. *Science,* **304,** 555–559.

——, and P. B. Rhines, 2009: Shifting surface currents in the northern North Atlantic Ocean. *J. Geophys. Res.,* **114,** C04005, doi:10.1029/2008JC004883.

Han, G., K. Ohashi, N. Chen, P. G. Myers, N. Nunes, and J. Fischer, 2010: Decline and partial rebound of the Labrador Current 1993-2004: Monitoring ocean currents from altimetric and conductivity–temperature–depth data. *J. Geophys. Res.,* **115,** C12012, doi:10.1029/2009JC006091.

Heimbach, P., C. Hill, and R. Giering, 2005: An efficient exact adjoint of the parallel MIT General Circulation Model, generated via automatic differentiation. *Future Gener. Comput. Syst.,* **21,** 1356–1371.

——, D. Menemenlis, M. Losch, J.-M. Campin, and C. Hill, 2010: On the formulation of sea-ice models. Part 2: Lessons from multi-year adjoint sea ice export sensitivities through the Canadian Arctic Archipelago. *Ocean Modell.,* **33** (1–2), 145–158.

Houghton, R., and M. Visbeck, 2002: Quasi-decadal salinity fluctuations in the Labrador Sea. *J. Phys. Oceanogr.,* **32,** 687–701.

Hurrell, J., cited 2008: NAO Index Data provided by the Climate Analysis Section. NCAR, Boulder, CO, digital media. [Available online at http://climatedataguide.ucar.edu/guidance/hurrell-north-atlantic-oscillation-nao-index-station-based.]

Ikeda, M., G. Symonds, and T. Yao, 1988: Simulated fluctuations in annual Labrador Sea ice cover. *Atmos.–Ocean,* **26,** 16–39.

——, T. Yao, and Q. Yao, 1996: Seasonal evolution of sea ice cover and shelf water off Labrador simulated in a coupled ice-ocean model. *J. Geophys. Res.,* **101** (C7), 16 465–16 489.

Kalnay, E., and Coauthors, 1996: The NCEP/NCAR 40-Year Reanalysis Project. *Bull. Amer. Meteor. Soc.,* **77,** 437–471.

Kitoh, A., S. Murakami, and H. Koide, 2001: A simulation of the last glacial maximum with a coupled atmosphere-ocean GCM. *Geophys. Res. Lett.,* **28,** 2221–2224.

Krahmann, G., and M. Visbeck, 2003: Arctic Ocean sea ice response to northern annular mode-like wind forcing. *Geophys. Res. Lett.,* **30,** 1793, doi:10.1029/2003GL017354.

Large, W., and S. Yeager, 2004: Diurnal to decadal global forcing for ocean and sea-ice models: The datasets and flux climatologies. CGD NCAR Tech. Note NCAR/TN-460+STR, 105 pp.

Lavender, K. L., R. E. Davis, and W. B. Owens, 2000: Mid-depth recirculation observed in the interior Labrador and Irminger seas by direct velocity measurements. *Nature,* **407,** 66–69, doi:10.1038/35024048.

——, ——, and ——, 2002: Observations of open-ocean deep convection in the Labrador Sea from subsurface floats. *J. Phys. Oceanogr.,* **32,** 511–526.

Losch, M., D. Menemenlis, J.-M. Campin, P. Heimbach, and C. Hill, 2010: On the formulation of sea-ice models. Part 1: Effects of different solver implementations and parameterizations. *Ocean Modell.,* **33** (1–2), 129–144.

Marsden, R., L. Mysak, and R. Myers, 1991: Evidence for stability enhancement of sea-ice in the Greenland and Labrador Seas. *J. Geophys. Res.,* **96** (C3), 4783–4789.

Marshall, J., A. Adcroft, C. Hill, L. Perelman, and C. Heisey, 1997a: A finite-volume, incompressible Navier Stokes model for studies of the ocean on parallel computers. *J. Geophys. Res.,* **102** (C3), 5753–5766.

——, C. Hill, L. Perelman, and A. Adcroft, 1997b: Hydrostatic, quasi-hydrostatic, and nonhydrostatic ocean modeling. *J. Geophys. Res.,* **102** (C3), 5733–5752.

McPhee, M. G., 1983: Turbulent heat and momentum transfer in the oceanic boundary layer under melting pack ice. *J. Geophys. Res.,* **88** (C5), 2827–2835.

——, G. Maykut, and J. Morison, 1987: Dynamics and thermodynamics of the ice-upper ocean system in the Marginal Ice Zone of the Greenland Sea. *J. Geophys. Res.,* **92** (C7), 7017–7031.

Menemenlis, D., and Coauthors, 2005: NASA supercomputer improves prospects for ocean climate research. *Eos, Trans. Amer. Geophys. Union,* **86,** 89–96, doi:10.1029/2005EO090002.

Morison, J. H., M. G. McPhee, and G. A. Maykut, 1987: Boundary layer, upper ocean, and ice observations in the Greenland Sea Marginal Ice Zone. *J. Geophys. Res.,* **92** (C7), 6987–7011.

Mysak, L. A., and D. K. Manak, 1989: Arctic sea-ice extent and anomalies, 1953-1984. *Atmos.–Ocean,* **27,** 376–405.

——, R. Ingram, J. Wang, and A. van der Baaren, 1996: The anomalous sea ice extent in Hudson Bay, Baffin Bay and the Labrador Sea during three simultaneous NAO and ENSO episodes. *Atmos.–Ocean,* **34,** 313–343.

National Oceanographic Data Center Operational Oceanography Group, 2008: Global temperature–salinity profile program. National Oceanographic Data Center. [Available online at http://www.nodc.noaa.gov/GTSPP/.]

Pickart, R. S., D. J. Torres, and R. A. Clarke, 2002: Hydrography of the Labrador Sea during active convection. *J. Phys. Oceanogr.,* **32,** 428–457.

Prinsenberg, S. J., I. K. Peterson, S. Narayanan, and J. U. Umoh, 1997: Interaction between atmosphere, ice cover, and ocean off Labrador and Newfoundland from 1962—1992. *Can. J. Fish. Aquat. Sci.,* **54,** 30–39.

Rogers, J. C., and H. Van Loon, 1979: The seesaw in winter temperatures between Greenland and Northern Europe. Part II: Some oceanic and atmospheric effects in middle and high latitudes. *Mon. Wea. Rev.,* **107,** 509–519.

Sathiyamoorthy, S., and G. Moore, 2002: Buoyancy flux at ocean weather station Bravo. *J. Phys. Oceanogr.,* **32,** 458–474.

Stern, H. L., and M. P. Heide-Jøargensen, 2003: Trends and variability of sea ice in Baffin Bay and Davis Strait, 1953–2001. *Polar Res.,* **22,** 11–18.

Straneo, F., R. Pickart, and K. Lavender, 2003: Spreading of Labrador Sea water: An advective-diffusive study based on Lagrangian data. *Deep-Sea Res. I,* **50,** 701–719.

Tang, C., 1992: Oceanographic features in the Newfoundland Marginal Ice Zone, March–April 1990. *Atmos.–Ocean,* **30,** 151–172.

Våge, K., and Coauthors, 2009: Surprising return of deep convection to the subpolar North Atlantic Ocean in winter 2007–2008. *Nat. Geosci.,* **2,** 67–72.

Visbeck, M., J. Fischer, and F. Schott, 1995: Preconditioning the Greenland Sea for deep convection: Ice formation and ice drift. *J. Geophys. Res.,* **100** (C9), 18 489–18 502.

Walsh, J. E., and C. M. Johnson, 1979: An analysis of Arctic sea ice fluctuations, 1953–77. *J. Phys. Oceanogr.,* **9,** 580–591.

Wunsch, C., 2006: *The Ocean Circulation Inverse Problem*. 1st ed. Cambridge University Press, 384 pp.

——, and P. Heimbach, 2007: Practical global oceanic state estimation. *Physica D,* **230** (1–2), 197–208.

Yao, T., and M. Ikeda, 1990: A model of sea ice and the upper ocean mixed layer off Labrador. *J. Geophys. Res.,* **95** (C7), 11 603–11 612.

Yashayaev, I., 2007: Hydrographic changes in the Labrador Sea, 1960–2005. *Prog. Oceanogr.,* **73,** 242–276.